Appl. Phys. A (2016) 122:351
DOI 10.1007/s00339-016-9862-8

Applied Physics A
Materials Science & Processing

Modal analysis of graphene microtubes utilizing a two-dimensional vectorial finite element method

Vasileios Salonikios[1] · Stamatios Amanatiadis[1] · Nikolaos Kantartzis[1] · Traianos Yioultsis[1]

Received: 11 August 2015 / Accepted: 14 November 2015 / Published online: 10 March 2016

Abstract The propagation properties of surface plasmon polariton waves on graphene microtubes were investigated in this paper. A precise vectorial finite element modal solver that models graphene as a surface boundary condition is devised for the graphene microribbon case. The solver extracts the dispersion curves through the effective index of various supported modes, while its propagation length, compared to the microstrip's one, unveils a notable behavior of surface waves. Also, radial and axial electric field components are evaluated at different frequencies, indicating the strong confinement at the surface of graphene and the impact of the microtubes' diameter on the propagating modes.

1 Introduction

Several studies have, recently, focused on graphene, the two-dimensional (2D) carbon allotrope [1], due to its unique wideband attributes [2–9]. Especially, at the far-infrared regime, the propagation of highly confined transverse magnetic (TM) surface plasmon polariton (SPP) waves is supported [10–13], permitting thus the design of efficient circuits [14–17]. The latter comprise, basically, graphene microribbons, which have been elaborately examined in previous studies through the propagation properties of the supported modes [18–21]. Actually, their straightforward planar implementation and preservation of the strong SPP confinement have enabled their use at several far-infrared applications. Nevertheless, the simultaneous propagation of two equally concentrated modes, i.e., the original waveguide and the edge one, with different properties, can degrade the overall operation, even at the lower THz frequencies.

For these reasons, the present paper studies the propagation properties of graphene microtubes, as an alternative means for the design of THz circuits. Initially, graphene's surface conductivity is described, and the key attributes of the surface wave are extracted for the infinite graphene layer case. To this goal, a 2D finite element modal solver, based on the vector wave Helmholtz differential equation, that models graphene as a surface boundary condition is developed. The accuracy of the featured solver in terms of the effective refractive index and electric field distribution (normal to the propagation plane) is verified via the popular microribbon setup. In addition, the extraction of the effective index for diverse modes at the far-infrared spectrum of the suggested structures reveals their significant behavior, which retains the desirable strong confinement of typical graphene geometries and improves the propagation length. Finally, a parametric study is conducted for different microtubes' diameters, keeping the curvature at acceptable levels to safely neglect quantum effects. The latter analysis indicates an important variation in the electric field distribution, which can be profitably exploited for the realization of advanced micronetworks.

2 Theoretical analysis

2.1 Surface conductivity of graphene

In our formulation, graphene is deemed an infinitesimally thin, two-sided layer determined by its surface conductivity

✉ Traianos Yioultsis
traianos@auth.gr

[1] Department of Electrical and Computer Engineering, Aristotle University of Thessaloniki, 54124 Thessaloniki, Greece

$\sigma(\omega, \mu_c, \Gamma, T)$, with ω the radial frequency, μ_c the chemical potential adjusted by an electrostatic bias voltage or chemical doping, Γ the energy-independent scattering rate, and T the temperature. Moreover, the conductivity of graphene is split at its two distinct contributions, i.e., the intraband and interband term, and is evaluated via the Kubo-based [22] expression of

$$\sigma_g(\omega,\mu_c,\Gamma,T) = \frac{je^2(\omega - j2\Gamma)}{\pi\hbar^2} \times \left[\frac{1}{(\omega - j2)^2}\int_0^\infty \varepsilon\left(\frac{\partial f_d(\varepsilon)}{\partial\varepsilon} - \frac{\partial f_d(-\varepsilon)}{\partial\varepsilon}\right)\mathrm{d}\varepsilon - \int_0^\infty \frac{f_d(-\varepsilon) - f_d(\varepsilon)}{(\omega - j2\Gamma)^2 - 4(\varepsilon/\hbar)^2}\,\mathrm{d}\varepsilon\right], \quad (1)$$

where e is the electron charge, $\hbar$ is the reduced Planck constants, and $f_d(\varepsilon)$ is the Fermi–Dirac distribution

$$f_d(\varepsilon) = \left(e^{\varepsilon - \mu_c/k_B T} + 1\right)^{-1}, \quad (2)$$

for k_B the Boltzmann constant. The frequency range in our analysis is limited at the far-infrared spectrum, where the interband term can be reliably ignored. Thus, only the intraband contribution is considered, computed by means of the following compact form

$$\sigma_g(\omega,\mu_c,\Gamma,T) = \frac{e^2 k_B T}{\pi\hbar^2(j\omega + 2\Gamma)}\left[\frac{\mu_c}{k_B T} + 2\ln\left(e^{-\mu_c/k_B T} + 1\right)\right]. \quad (3)$$

In this context, the complex wave number of the SPP wave k_ρ, in the vacuum, is theoretically calculated in terms of graphene's surface conductivity through

$$k_\rho = k_0\sqrt{1 - 4/(\eta_0\sigma_g)^2}, \quad (4)$$

where k_0 and η_0 are the vacuum wave number and wave impedance [10], respectively. Then, the effective index n_{eff} of the surface wave, defined as the SPP wave number normalized to the vacuum one, can be extracted as

$$n_{\mathrm{eff}} = k_\rho/k_0 = \sqrt{1 - 4/(\eta_0\sigma_g)^2}. \quad (5)$$

On the other hand, the surface wave propagation length L_{SPP}, specified as the distance required for the SPP intensity to decay by a factor of $1/e$, is evaluated in terms of the imaginary part of k_ρ through

$$L_{\mathrm{SPP}} = \Im\{1/(2k_\rho)\}. \quad (6)$$

2.2 Development of the finite element modal solver

To examine the properties of graphene microtubes, a vectorial finite element (FE) modal solver is developed. Based on the general concept of [23], the computational domain is defined as the transverse plane on the propagation axis, which coincides with that of the microtube. In this manner, our formulation stems from the vector wave Helmholtz partial differential equation, with the electric field as its working variable, i.e.,

$$\nabla\times(\hat{\mu}_r\nabla\times\mathbf{E}) - k_0^2\hat{\varepsilon}_r\mathbf{E} = 0, \quad (7)$$

where $\hat{\mu}_r$ and $\hat{\varepsilon}_r$ are the relative permeability and permittivity tensors, respectively, supporting the anisotropy of the involved media. First, the transverse electric field components are expanded via continuous vector basis functions, while the remaining axial one is treated via node-based scalar basis functions [24]. To discretize (7), we implement the Galerkin approximation, which leads to the weak formulation of

$$\iint_S(\nabla\times\mathbf{U})\hat{\mu}_r^{-1}(\nabla\times\mathbf{E})\mathrm{d}S - k_0^2\iint_S\mathbf{U}\hat{\varepsilon}_r\mathbf{E}\mathrm{d}S + \oint_{\partial S}(\hat{\mathbf{n}}\times\hat{\mu}_r^{-1}\nabla\times\mathbf{E})\mathbf{U}\mathrm{d}\ell = 0, \quad (8)$$

with S the computational space truncated by a suitably tailored perfectly matched layer (PML), ∂S the enclosing boundary, $\hat{\mathbf{n}}$ its normal unit vector, and $\mathbf{U}$ the adjoint field. In this context, the resulting system constitutes a quadratic eigenvalue problem, transformed to a linear one, pertinent for sparse eigensolvers that employ the first companion linearization technique.

A significant feature of the proposed algorithm in terms of accuracy and simplicity is the incorporation of graphene's contribution. This is attained via a surface current density $\mathbf{J}_s = \sigma_s\mathbf{E}_s$ in the form of a finite conductivity boundary condition. The latter is applied exclusively at the degrees of freedom that are tangential to the one-dimensional curve created by the intersection of graphene's surface with the computational plane, as shown in Fig. 1. Hence, the domain is enclosed by a non-unified boundary, consisting of both the aforesaid condition and a perfectly electric conductor boundary that terminates the PML. In particular, this finite conductivity boundary condition is evaluated by

$$\hat{\mathbf{n}}_g\times(\mathbf{H}^+ - \mathbf{H}^-) = \mathbf{J}_s, \quad (9)$$

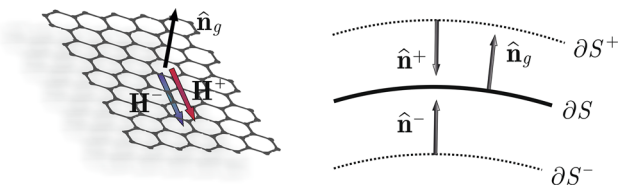

Fig. 1 Surface boundary condition formulated in terms of the magnetic field and the normal, to the graphene's surface, unitary vector (due to the surface conductivity of graphene)

$$\frac{j}{\omega\mu_0}\hat{\mathbf{n}}_g \times (\nabla \times \mathbf{E}^+ - \nabla \times \mathbf{E}^-) = \sigma_s \mathbf{E}_s, \tag{10}$$

$$\hat{\mathbf{n}}_g \times \nabla \times \mathbf{E}^+ - \hat{\mathbf{n}}_g \times \nabla \times \mathbf{E}^- = -j\omega\mu_0\sigma_s \mathbf{E}_s, \tag{11}$$

$$\hat{\mathbf{n}}^+ \times \nabla \times \mathbf{E}^+ + \hat{\mathbf{n}}^- \times \nabla \times \mathbf{E}^- = j\omega\mu_0\sigma_s \mathbf{E}_s. \tag{12}$$

Then, (9)–(12) are embedded in the FE system via the line integral term of (8), as

$$\begin{aligned}\oint_{\partial S} (\hat{\mathbf{n}} \times \nabla \times \mathbf{E})\mathbf{U}\mathrm{d}\ell &= \int_{\partial S^+} \mathbf{U}\hat{\mathbf{n}}^+ \times \nabla \times \mathbf{E}^+ \mathrm{d}\ell + \int_{\partial S^-} \mathbf{U}\hat{\mathbf{n}}^- \times \nabla \times \mathbf{E}^- \mathrm{d}\ell \\ &= j\omega\mu_0 \int_{\partial S} \mathbf{U}\sigma_s \mathbf{E}_s \mathrm{d}\ell.\end{aligned} \tag{13}$$

Alternatively, graphene may be considered as a bulk medium, implying that its conductivity is included in the complex relative dielectric permittivity ε_r^*, to obtain

$$\varepsilon_r^* = \varepsilon_r - j\sigma_s/(\omega\varepsilon_0). \tag{14}$$

Since σ_s has both real and imaginary parts, the real part of (14) is ignored and graphene's contribution is inserted in (8) through its second surface integral term [25]. However, as graphene is considered infinitesimally thin, the variation in the integrated quantities in this surface integral is negligible along one dimension, implying that the latter degenerates to a line integral, computed only for the tangential to the graphene's surface degrees of freedom. In this way, the previous interpretation of graphene's contribution leads to (8), as well.

Then, the expansion of the described weak formulation (13) yields the generalized eigenvalue problem of

$$\begin{bmatrix} 0 & 0 & \mathbf{I} & 0 \\ 0 & 0 & 0 & \mathbf{I} \\ \mathbf{M}_t & 0 & 0 & \mathbf{P} \\ 0 & \mathbf{M}_z & \mathbf{Q} & 0 \end{bmatrix} \begin{bmatrix} E_t \\ E_z \\ n_{\mathrm{eff}}E_t \\ n_{\mathrm{eff}}E_z \end{bmatrix} = n_{\mathrm{eff}} \begin{bmatrix} \mathbf{I} & 0 & 0 & 0 \\ 0 & \mathbf{I} & 0 & 0 \\ 0 & 0 & \mathbf{T}_t & 0 \\ 0 & 0 & 0 & 0 \end{bmatrix} \begin{bmatrix} E_t \\ E_z \\ n_{\mathrm{eff}}E_t \\ n_{\mathrm{eff}}E_z \end{bmatrix} \tag{15}$$

$$[A][x] = n_{\mathrm{eff}}[B][x], \tag{16}$$

where the eigenvalue of the problem is the complex effective refractive index n_{eff} of the propagation mode and column vector $[x]$ is the corresponding eigenvector. Furthermore, the elements of matrices $[A]$ and $[B]$ are the block matrices obtained from the assembly of the integral terms in (13) for every element. Conversely, the line integral terms, due to the surface treatment of graphene, are contained in block matrices $\mathbf{M}_t$ and $\mathbf{M}_z$.

3 Numerical results

3.1 Modal solver verification

Firstly, we examine the well-documented case of the graphene microribbon, in order to demonstrate the validity of the vectorial FE modal solver. Particularly, our interest focuses on the free-standing microribbon with a width of 5 μm, and graphene parameters selected as $\mu_c = 0.2$ eV, $\Gamma = 0.1$ meV at room temperature $T = 300$ K. Figure 2 depicts the dispersion diagram of the first three modes, compared to the theoretical dispersion relation of the infinite layer case, computed through (5). The higher effective index at the microstrip modes is related to the confinement of moving charges, hence a more inductive behavior that is in full compliance with the existing literature [19]. Moreover, the distribution of the normal and tangential, to the graphene's surface, electric field component is illustrated in Fig. 3, proving the concentration at the microribbon edges and verifying the accuracy of the vectorial FE solver.

3.2 Graphene microtube analysis

The ability of the featured methodology to model arbitrary geometries is exploited via the treatment of graphene

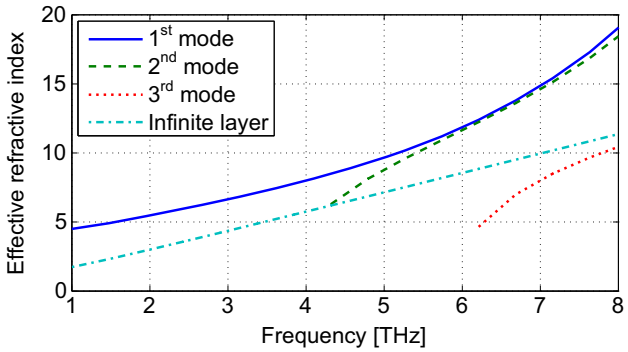

Fig. 2 Dispersion curves of the first three modes on a graphene microribbon with a width of 5 μm, compared to that of the infinite layer case

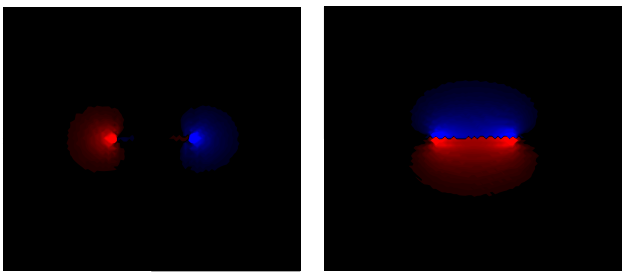

Fig. 3 Distribution of the tangential E_x (*left*) and normal E_y (*right*), to the 5 μm-wide graphene microribbon, electric field component at 3 THz

microtubes. An indicative computational domain terminated by PMLs is given in Fig. 4, where, in the vicinity of the microtube, the mesh is much more refined than the rest of the space. Overall, the discretization involves approximately 75,000 elements and 15×10^4 unknown freedom coefficients. In this framework, several graphene microtubes with different diameters are explored at the far-infrared spectral range, regarding their plasmonic modes and sorted according to their corresponding losses, namely the imaginary part of the matching eigenvalue. Note that graphene parameters remain the same as those of the previous section.

Based on these aspects, an infinitely long 20 μm-diameter graphene microtube is considered and its dispersion diagram for the first four modes is displayed in Fig. 5. Mainly, a behavior similar to the SPP modes propagating on an infinite graphene layer can be detected, since n_{eff} increases linearly with frequency. Furthermore, the dispersion curves of the second and third modes are in close proximity, revealing a degenerate mode attributed to the obvious cylindrical symmetry of the problem. This deduction is supported by examining the electric field distribution of Fig. 6, at 2 THz. In essence, the degeneracy of the second and third modes is evident from their field patterns, as they are complementary; thus, only the second mode is taken into account for the rest of our study. Also, all modes are confined laterally on the graphene's surface, presenting a TM profile, with the radial component E_ρ as

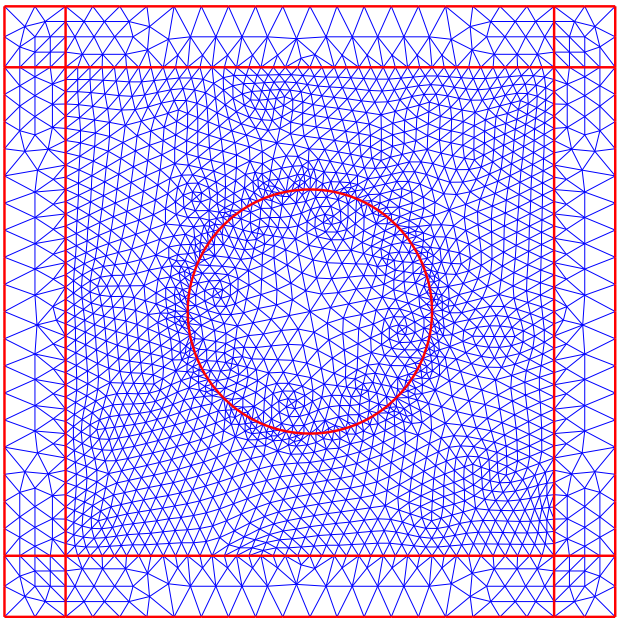

Fig. 4 Computational domain of the graphene microtube

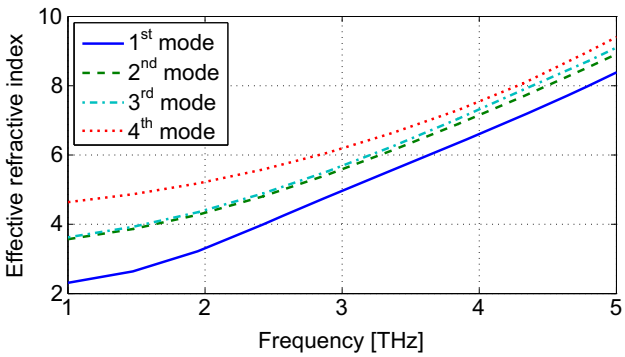

Fig. 5 Dispersion curves of the first four modes on a graphene microtube with a diameter of 20 μm

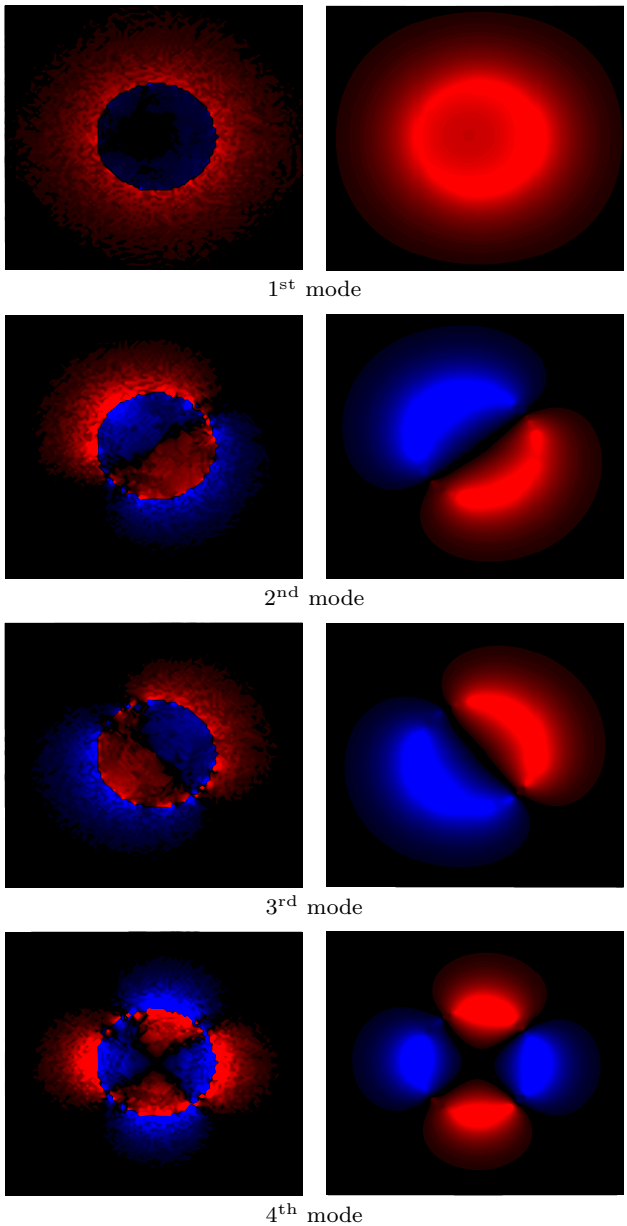

Fig. 6 Distribution of the radial E_ρ (*left*) and the axial E_z (*right*), to the propagation, electric field components for the first four modes on a graphene microtube with a diameter of 20 μm at 2 THz

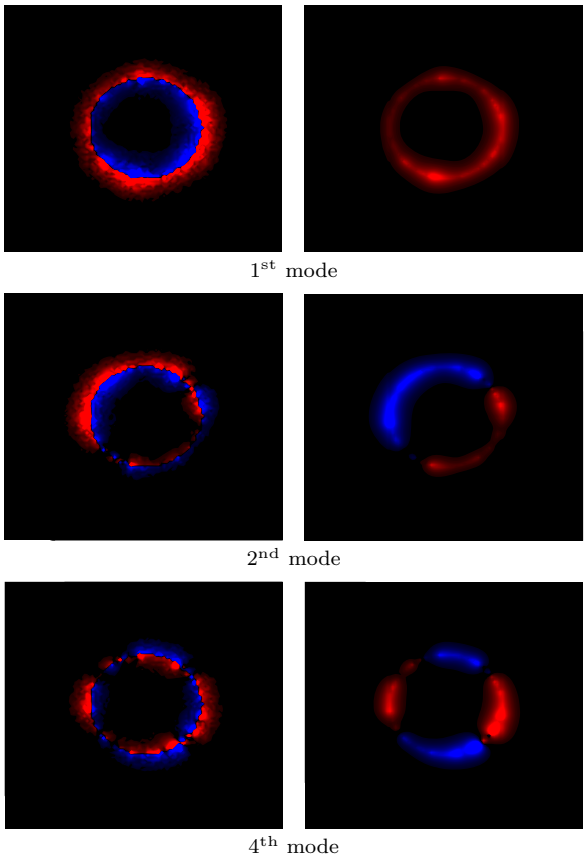

Fig. 7 Distribution of the radial E_ρ (*left*) and the axial E_z (*right*), to the propagation, electric field components for the first three modes on a graphene microtube with a diameter of 20 μm at 4 THz

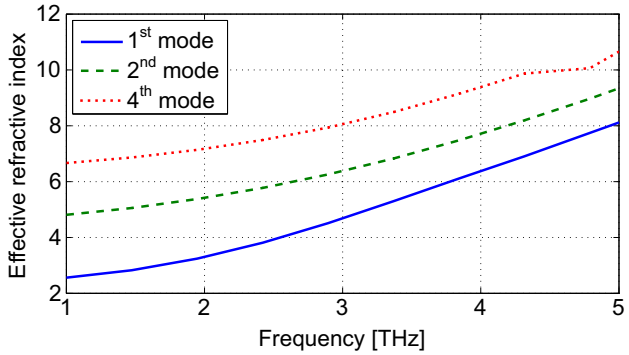

Fig. 8 Dispersion curves of the first three modes on a graphene microtube with a diameter of 10 μm

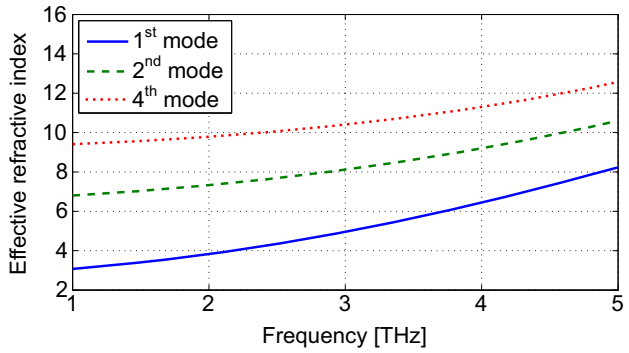

Fig. 9 Dispersion curves of the first three modes on a graphene microtube with a diameter of 5 μm

the dominant one, since it is normal to the graphene's surface. Another interesting observation is that the first mode presents a monopole behavior, the second that of a dipole, and the fourth a quadrupole one. On the other hand, inspecting the electric field distribution of Fig. 7 at the higher frequency of 4 THz, we can securely claim that field confinement increases with frequency, as theoretically expected.

Proceeding to microtubes with gradually smaller diameters, dispersion diagrams for 10 and 5 μm are, respectively, plotted in Figs. 8 and 9, where the curvature remains at reasonable levels and quantum effects can be reliably ignored. It may be observed that n_{eff}, and thus the confinement, augments as the diameter reduces, which is clearer for the fourth mode and less prominent for the second one. This issue prompts us to further inspect the case of 5 μm, by providing its electric field distribution in Fig. 10 at 2 THz, in order to be comparable with the 20 μm one. Obviously, the two patterns have significant similarities, while the confinement on the surface of graphene is slightly increased at the smaller microtube, thus verifying our dispersion diagrams. In addition, the propagation length is extracted through the n_{eff} imaginary part and illustrated in Fig. 11, for the first three modes of the 5 μm-wide microtube and the first mode of the 5 μm-long microribbon. Comparing the attenuation of the first modes, it becomes apparent that the microtube presents an adequately larger propagation length, offering enhanced and instructive propagation characteristics.

Finally, since the existence of SPP modes in microtubes has been successfully determined, we explore a graphene microtube with a diameter of 5 μm and a silica core of relative dielectric permittivity $\varepsilon_r = 3.32$. The resulting dispersion diagram is given in Fig. 12, where it appears that the insertion of the silica core increases the effective indices of all three dispersion curves. Actually, this outcome is deemed promising for the potential use of such structures as an alternative means in the systematic design of efficient high-end micronetworks.

4 Conclusions

The propagation properties of SPP waves on graphene microtubes have been comprehensively investigated in this paper by means of a flexible 2D vectorial FE modal solver.

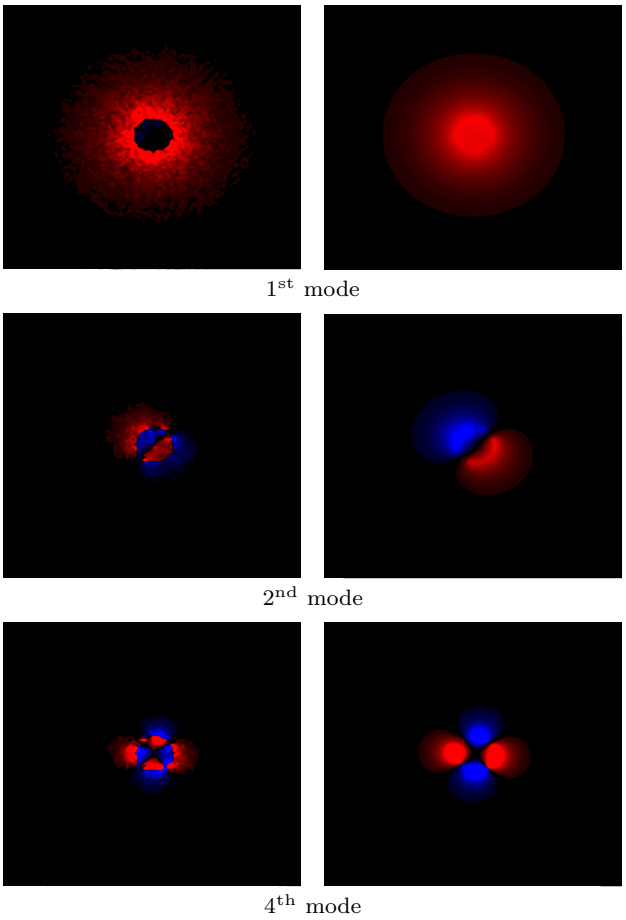

Fig. 10 Distribution of the radial E_ρ (*left*) and the axial E_z (*right*), to the propagation, electric field component for the first three modes of a graphene microtube with a diameter of 5 μm at 2 THz

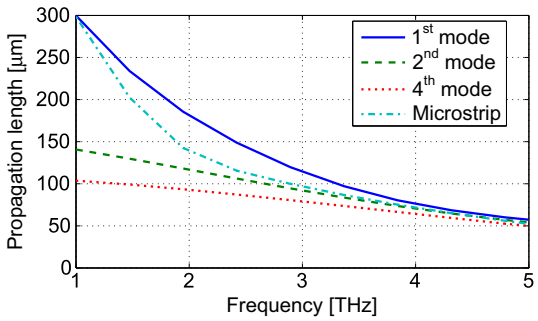

Fig. 11 Propagation length of the SPP wave for the first three modes on a graphene microtube with a diameter of 5 μm, compared to that of the first mode on a microstrip with a width of 5 μm

After the formulation of the graphene surface conductivity model and its insertion on the prior solver, a microribbon setup has been utilized to validate the proposed technique. Therefore, the propagation properties of various modes on several microtubes have been carefully studied through

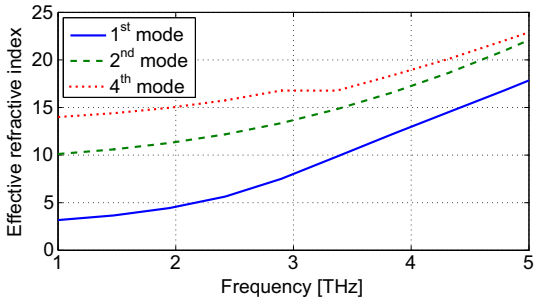

Fig. 12 Dispersion curves of the first three modes on a graphene microtube with a diameter of 5 μm and a silica core

dispersion diagrams and the associated electric field distributions, indicating a better confinement at decreased diameters. Furthermore, the propagation length of the graphene microtube has been compared to the microribbon one, exhibiting an optimal behavior, able to enhance the development of plasmonic circuits at the far-infrared regime.

References

1. A. Geim, K. Novoselov, J. Appl. Phys. **103**, 064302 (2008)
2. F. Bonaccorso, Z. Sun, T. Hasan, A. Ferrari, Nat. Photon. **4**, 611–622 (2010)
3. A.S. Mayorov, R.V. Gorbachev, S.V. Mozorov, L. Britnell, R. Jalil, L.A. Ponomarekno, P. Blake, K.S. Novoselov, K. Watanabe, T. Taniguchi, A.K. Geim, Nano Lett. **11**, 2396–2399 (2011)
4. Y. He, W. Huang, Y. Yang, C. Li, Appl. Phys. A **106**, 41–46 (2012)
5. H. Xu, W. Lu, W. Zhu, Z. Dong, T. Cui, Appl. Phys. Lett. **100**, 243110 (2012)
6. A. Andryieuski, A. Lavrinenko, Phys. Rev. B **86**, 121108 (2012)
7. H. Lin, M. Hung, C. Huang, H. Chui, J. Lin, Appl. Phys. A **115**, 399–402 (2014)
8. J. Wu, Q. Huang, Appl. Phys. A **116**, 1747–1756 (2014)
9. I. Chang, J. Chen, Appl. Phys. A **119**, 265–274 (2015)
10. G.W. Hanson, J. Appl. Phys. **103**, 064302 (2008)
11. V. Kaushik, A.K. Shukla, V.D. Vankar, Appl. Phys. A **117**, 2197–2205 (2014)
12. A. Grigorenko, M. Polini, K. Novoselov, Nat. Photon. **6**, 749–758 (2012)
13. Z.H. Yang, C.C. Guo, K. Liu, J.F. Zhang, W.M. Ye, X.D. Yuan, S.Q. Qin, Appl. Phys. A **114**, 1017–1021 (2014)
14. A. Vakil, N. Engheta, Phys. Rev. B **85**, 075434 (2011)
15. P. Yang, X. Li, H. Yang, Y. Tang, X. Yuan, Appl. Phys. A **112**, 759–765 (2013)
16. P. Chen, H. Huang, D. Akinwande, A. Alù, ACS Photon. **1**, 647–654 (2014)
17. W.-J. Gong, L.-H. Jin, X. Sun, Y. Han, Appl. Phys. A **118**, 1211–1217 (2015)
18. S. Mikhailov, K. Ziegler, Phys. Rev. Lett. **99**, 016803 (2007)
19. A. Nikitin, F. Guinea, F. García-Vidal, L. Martín-Moreno, Phys. Rev. B **84**, 161407(R) (2011)
20. X.-H. Jia, H.-J. Song, C.-Y. Min, X.-Q. Zhang, Appl. Phys. A **109**, 261–265 (2013)

21. X. Wang, M. Yu, W. Zhang, B. Zhang, L. Dong, Appl. Phys. A **118**, 1053–1058 (2015)
22. V. Gusynin, S. Sharapov, J. Carbotte, J. Phys. Cond. Mat. **19**, 026222 (2007)
23. S. Selleri, L. Vincetti, A. Cucinotta, M. Zoboli, Opt. Quantum Electron. **33**, 359–371 (2001)
24. J.-M. Jin, *The Finite Element Method in Electromagnetics*, 3rd edn. (Wiley, New York, 2014)
25. I. Dermitzioglou, T. Yioultsis, in *Proceedings of the 36th Progress in Electromagnetics Research Symposium (Prague, 2015)*, pp. 2201–2205